



Oceanic basement roughness in the central Red Sea

[Link to publication record in Manchester Research Explorer](#)

Citation for published version (APA):

Shi, W., Mitchell, N., Kalnins, L. M., Stewart, I. C. F., & Izzeldin, A. Y. (Accepted/In press). Oceanic basement roughness in the central Red Sea. In N. M. A. Rasul, & I. C. F. Stewart (Eds.), *Rifting and sediments in the Red Sea and Arabian Gulf regions* Taylor & Francis.

Published in:

Rifting and sediments in the Red Sea and Arabian Gulf regions

Citing this paper

Please note that where the full-text provided on Manchester Research Explorer is the Author Accepted Manuscript or Proof version this may differ from the final Published version. If citing, it is advised that you check and use the publisher's definitive version.

General rights

Copyright and moral rights for the publications made accessible in the Research Explorer are retained by the authors and/or other copyright owners and it is a condition of accessing publications that users recognise and abide by the legal requirements associated with these rights.

Takedown policy

If you believe that this document breaches copyright please refer to the University of Manchester's Takedown Procedures [<http://man.ac.uk/04Y6Bo>] or contact uml.scholarlycommunications@manchester.ac.uk providing relevant details, so we can investigate your claim.



Chapter 11: Oceanic basement roughness in the central Red Sea

Authors:

Wen Shi (Department of Earth and Environmental Sciences, The University of Manchester, Manchester M13 9PL, UK, now at: Institute of Geophysics, China Earthquake Administration, Beijing 100081, China, mjshiwen@gmail.com)

*Neil C. Mitchell (Department of Earth and Environmental Sciences, The University of Manchester, Manchester M13 9PL, UK, Neil.Mitchell@manchester.ac.uk)

Lara M. Kalnins (School of GeoSciences, The University of Edinburgh, The King's Buildings, Edinburgh, EH9 3FE, UK)

Ian C.F. Stewart (Stewart Geophysical Consultants Pty. Ltd., Adelaide, South Australia, stewgeop@senet.com.au)

A.Y. Izzeldin (Awasconrc, Gereif W, H4, Bld 376, Khartoum, POB 410, Khartoum, Sudan)

This is the green open-access version of the above-title chapter accepted for publication on 10 July 2022 in the book "Rifting and sediments in the Red Sea and Arabian Gulf regions", edited by N.M.A. Rasul and I.C.F. Stewart, to be published by Taylor & Francis Ltd.

Abstract

The Red Sea is a rare example of a continental rift proceeding to an oceanic basin. In the central Red Sea, the transition to oceanic spreading appears to have occurred at ~10 Ma, but unusually low frequencies of magnetic anomalies suggest that spreading may have occurred in spreading centres that were buried beneath the evaporites before ~5 Ma. We continue our investigation of this area by assessing the basement roughness (the root-mean-square variation of basement relief) along profiles across and parallel to the spreading axis. The across-axis roughness can be compared with that of typical abyssal hill topography formed by faulting and volcanism, whereas the axis-parallel roughness can be compared with variations due to the ridge segmentation. We estimated roughness values from depths of basement interpreted from across-ridge seismic reflection profiles. The best estimate of mean across-ridge roughness of 230 m overlaps with, but is generally smaller than, those observed over ultraslow spreading ridges, consistent with a ridge affected by a hotspot (here the Afar), which typically leads to smaller fault relief. Basement roughness values along ridge-parallel profiles were computed from the free-air gravity field using densities appropriate for oceanic crust and a modified Bouguer slab formula, since suitable ridge-parallel seismic profiles are not available. Errors arising from the slab approximation were investigated using forward 2D modelling and found to be ~30%. Correcting for this bias leaves roughness values within the range of values for the ultra-slow spreading Southwest Indian Ridge, which appears organised into segments due to magmatism concentrated at segment centres. Such an organisation has been suggested for the central Red Sea previously based on the segmented structure of gravity anomalies. The axis-parallel roughness values reach minima roughly mid-way between the coast and the axial trough, where the suggested transition from stretched continental to

predominantly oceanic crust occurs. The basement relief due to ridge segmentation therefore appears to have grown gradually since continental breakup.

11.1 Introduction

The Red Sea is currently transitioning from continental rifting to oceanic seafloor spreading (Cochran 1983; Cochran and Martinez 1988; Rihm and Henke 1998). Whether the crust in the central Red Sea (Figure 11.1) is continental or oceanic has been debated (Bonatti 1985; Ligi et al. 2012; Mitchell and Park 2014; Shi et al. 2018) because the crust is buried under Miocene evaporites that reach kilometres in thickness and is thus inaccessible. However, the following evidence now points to it being largely oceanic and created since ~10 Ma. Shi et al. (2018) found an oceanic-like axial crustal high in the central Red Sea after correcting seismically derived basement depths (Izzeldin 1982) for isostatic loading by evaporites and other sediments. They suggested that the axis of the central Red Sea rift is an ultra-slow spreading mid-ocean ridge affected by the Afar hotspot, like the Reykjanes Ridge, an axial high formed by the Iceland hotspot. They also found a simple correlation between Bouguer gravity anomalies and basement depths to ~60-80 km from the spreading axis as expected of oceanic crust but a dramatically weaker correlation nearer to the continents, suggesting a change there to a low-density structure, i.e., continental crust. The transition coincides with changes in crustal seismic velocities (Tramontini and Davies 1969; Davies and Tramontini 1970; Egloff et al. 1991). Symmetrical pairs of anomalies, which are indicative of oceanic crust (Hall, 1989), can be observed around the central Red Sea spreading axis to about this transition, thus dating it at 10 Ma (Mitchell et al. 2021; Okwokwo et al. 2022). However, those

anomalies vary in spatial frequency, with high-frequency anomalies typical of normal seafloor spreading present to ~5 Ma but much smoother, low-frequency anomalies on crust older than 5 Ma. Okwokwo et al. (2022) interpreted the change at 5 Ma as the point at which the spreading centres became exposed to seawater after previously being buried under the evaporites (when spreading more typically involved volcanic intrusions rather than extrusions). This raises the question of what structure the spreading ridge had when buried and later exposed.

Basement roughness is defined as the root-mean-square deviation of residual basement relief along a profile after removal of systematic trends (Malinverno 1991). The roughness can provide observational constraints on changes in crustal thickness and tectonics (Ma and Cochran 1997). Basement roughness has been used in investigations of crustal structure, spreading rate, faulting models, and ridge morphology at mid-ocean ridges (e.g., Bird and Pockalny 1994; Malinverno and Gilbert 1989; Minshull 1999; Sauter et al. 2018; Small 1994). Sauter et al. (2011, 2018) suggested that spreading rate, mantle temperature, and lithosphere composition could affect the lithospheric strength and thus the basement roughness. Sauter et al. (2018) characterized roughness of oceanic basement in deep seismic reflection data from margins formed at a wide range of plate-tectonic opening rates. Although those results using across-margin profiles did not reveal the nature of transitions in roughness across the continent-ocean boundaries, they showed that the early formed oceanic crust had roughnesses typical of oceanic crust formed at more mature ridges with similar spreading rates.

In this study, we have computed basement roughness values in the central Red Sea along lines both parallel to the axis and across the axis in order to assess how basement roughness compares with those of other mid-ocean ridges. Due to the presence of a prominent axial ridge in across-axis seismic profiles, simple detrending used in previous analyses is not possible. However, using a frequency filtering approach to remove the effect of the ridge, we find comparable roughness values to a compilation of Sauter et al. (2018). Furthermore, the along-axis roughness values, which were computed by inversion of the free-air gravity anomalies, reach minima at the continent-ocean boundary, suggesting that basement relief due to the new oceanic segmentation took a finite time to become established after the transition.

11.2 Tectonic setting

The Red Sea is a young ocean basin formed by the Arabian plate separating from the Nubian plate (Ghebreab 1998; McKenzie et al. 1970). It is one of the few places on Earth where a geologically recent or active transition from continental extension to seafloor spreading can be observed (Cochran and Martinez 1988; Rihm and Henke 1998). The extension forming the Red Sea may have first started in the Eocene and became faster in the Oligocene at ~ 30 Ma (Bosworth and McClay 2001; Hofmann et al. 1997; Mohr 1983; Omar and Steckler 1995). The 0-3 Ma Red Sea spreading rate increases southward from ~ 10 mm yr⁻¹ at 25.5°N to ~ 16 mm yr⁻¹ near 18°N (Chu and Gordon 1998; DeMets et al. 1990, 2010; Reilinger et al. 2015).

The southern Red Sea (south of 19°N; Figure 11.1) has a well-developed continuous axial zone, with volcanic geomorphology in multibeam data, large amplitude magnetic anomalies and basaltic lavas recovered in dredges as evidence of extensive

volcanism (Augustin et al. 2014; Haase et al. 2000; Phillips 1970; Roeser 1975). Ocean floor magnetic anomalies in the southern Red Sea are clearly identifiable up to Chron 3A, suggesting that full seafloor spreading started at least by 5 Ma (Cochran 1983; Girdler and Styles 1974; Phillips 1970; Roeser 1975; Vine 1966). Based on spreading rates of Chu and Gordon (1998) and locations of volcanic ridges, Augustin et al. (2014, 2016) suggested that seafloor spreading began at 8–12 Ma, with some older oceanic crust buried under the thick Miocene evaporites (Girdler 1984; Girdler and Whitmarsh 1974).

A series of closed-contour depressions known as ‘deeps’ occur in the central Red Sea between 19°N and 23°N (Figure 11.1) (Bonatti 1985; Pautot et al. 1984). High amplitude magnetic anomalies, volcanic geomorphology and normal mid-ocean ridge basalt (MORB) suggest that they are underlain by oceanic spreading centres (Augustin et al. 2014, 2016; Bonatti 1985; Izzeldin 1987; Pautot et al. 1984). However, the nature of the crust underlying the shallower inter-trough zones (areas between the deeps) and off-axis flanks, which are both covered by evaporites and hemipelagic sediments, has been more controversial. Some authors have interpreted the low amplitude magnetic anomalies found in the inter-trough zones and off-axis as indicating a highly extended continental crust (Bonatti 1985; Cochran and Karner 2007; Ligi et al. 2011, 2012). However, as mentioned earlier, oceanic crust is now preferred based on the basement axial high, parallel and symmetrical magnetic anomalies and segmented structure of the free-air gravity field. The low amplitude magnetic anomalies can be explained by the ultra-slow spreading rates, the magnetic source layer being deeper than for an exposed ridge (Dyment et al. 2013; Okwokwo et

al. 2022), or effects of alteration (Levi and Riddihough; Augustin et al. 2014, 2016) or intrusions (Dyment et al. 2013; Okwokwo et al. 2022) under the evaporites.

In the northern Red Sea (north of 23°N; Figure 11.1), the deeps are less pronounced and become more widely spaced, although basaltic lavas have been recovered from them (Bonatti 1985; Cochran 2005; Guennoc et al. 1988; Pautot et al. 1984). The presence of large fault blocks of continental crust has been inferred from the gravity anomalies combined with seismic refraction data (Cochran and Karner 2007; Martinez and Cochran 1988). In contrast, others have suggested this region is also underlain by oceanic crust based on unpublished seismic reflection and magnetic data (Dyment et al. 2013; Tapponnier et al. 2013). From reconstructions of geological features across the Red Sea, Sultan et al. (1992, 1993) and Kozdroj et al. (2012) suggested that the entire Red Sea basin is underlain by oceanic crust.

In this chapter, we focus on the central Red Sea where the structure appears now more straightforward. We derive basement roughness values from seismic reflection lines across the axis and from gravity lines parallel to the axis. The former values are typical of oceanic crust created at slow or ultra-slow rates, whereas the latter are also typical of such oceanic crust though additionally reveal a transition across the continent-ocean boundary.

11.3 Data and methods

11.3.1 Seismic reflection

Multichannel seismic reflection data used in this study were collected in 1976 (Izzeldin 1982, 1987) using a Vaporchoc source with a 2.4 km streamer consisting of 48 channels in deep waters and with a 24-channel 1.2 km streamer in shallow waters. The data were processed using a 24-fold stack, with stacking velocities computed every 3.6 km along track. The locations of seismic reflection profiles 7, 9, 11, 15, 17, 19, 21, 25, 27, 29, and 31 are shown in Figures 11.2a and 11.2b. These data are unfortunately now only available as paper records.

Basement depths were derived from these data as described by Shi et al. (2018). They converted two-way travel times of the basement and seabed reflections to depths below sea level using P-wave velocities (V_p) of 1.538 km s⁻¹, 1.9 km s⁻¹, and 4.21 km s⁻¹ for water, Plio-Pleistocene sediments, and evaporites, respectively. Figure 11.3 shows those depths.

The basement depths corrected for isostatic loading of the evaporites and other sediments by Shi et al. (2018) were used here to estimate basement roughness along the seismic profiles. Previous work has simplified the topography of oceanic basement by considering it as comprising a component that varies systematically with basement age mainly due to lithospheric cooling (a deterministic component) and a component that varies stochastically, i.e., the basement roughness (Goff and Jordan 1988; Malinverno 1991). Removing the systematic trend from basement elevation data leaves the stochastic component, which can then be characterized. For example, Malinverno (1991) subtracted a linear trend from segments of bathymetry data and calculated root-mean square variations of the residuals.

In the central Red Sea, the oceanic crust is young (mostly <10 Ma) and the basement forms an axial high whose shape varies among the profiles crossing it (Figure 11.3). The decline in basement elevation from the axis to 60-80 km off-axis is too rapid to be caused only by lithospheric cooling, even after allowing for isostatic loading by the evaporites (Shi et al. 2018). It may include effects of mantle melting and crustal emplacement of magmas that vary among the profiles. If that is the case, it is not feasible to remove a uniform systematic variation. Furthermore, the oceanic crust is only ~100-160 km across.

It was decided to include the ridge crest in the analysis and use a running median average to derive a systematic variation for each profile and then remove it from the data series. For example, the residual basement reliefs in [Figure 11.4c](#) were obtained by removing the regional variation of [Figure 11.4b](#) from the basement depths in [Figure 11.4a](#). Root-mean-square variations of those residual reliefs were then computed to represent the roughness. As the roughnesses were computed by a different method from previous studies, the values need to be compared bearing in mind this difference. The results are also non-unique; [Figure 11.4d](#) shows how the basement roughness varies with filter width. After experimenting with various filter widths, 60 km appears to do a good job of attenuating most of the abyssal hill topography while still recording the regional variation ([Figure 11.4b](#)). Removing that low-pass filtered topography then leaves the abyssal hill topography or basement roughness ([Figure 11.4c](#)). Furthermore, the roughness in [Figure 11.4d](#) varies gradually with filter width so it is insensitive to the chosen width. In [Figure 11.5](#), the value obtained with the 60 km filter width is shown with the red star, whereas the

error bar (120 to 460 m) represents the effect of filter width varying from 0 to 240 km, a highly conservative range.

11.3.2 Gravity anomalies

11.3.2.1 *Free-air gravity data*

We have used version 23 of the marine gravity field (referred to as “SSv23”) derived from satellite altimetry measurements by Sandwell et al. (2014). The data are shown in Figure 11.2a.

Shipboard gravity data obtained from the National Centers for Environmental Information (NCEI) (www.ngdc.noaa.gov/mgg) were used to evaluate the SSv23 data. These data were collected on RRS *Shackleton* in 1987 with a LaCoste and Romberg gravity meter (Girdler and Southren 1987) and on RV *Robert Conrad* during cruise RC2507 in 1984 with a Bell BGM-3 gravity meter (Cochran and Martinez 1988).

Some spikes occur in shipboard datasets, e.g., due to errors in Eötvös correction and centripetal accelerations occurring with course changes (Mitchell 2015; Wessel and Watts 1988). A 4-km running median average filter was found to remove the outliers from the shipboard values effectively, while also smoothing the data over a length-scale still within the resolution of the gravity data and of the navigation used in the RRS *Shackleton* cruise. After applying that filter, the two datasets (SSv23 and

filtered shipboard data) were differenced and distributions of their differences constructed (Figures 11.6 and 11.7).

The differences between the SSv23 and the RRS *Shackleton* and RV *Robert Conrad* data have standard deviations of 5.5 and 3.7 mGal (Figure 11.6). The RV *Robert Conrad* data more closely follow SSv23 than the RRS *Shackleton* data, most likely because of the superior Bell BGM-3 gravity meter on the RV *Robert Conrad* cruise (Mitchell 2015). In the map of the differences (Figure 11.7), blue areas indicate that SSv23 is ~10 or more mGal smaller than the shipboard values on the eastern side between 25°N and 26 °N, and near the centre at 24 °N and 20 °N. These differences are larger than anomalies in other evaluations (Sandwell et al. 2013) and their origins are difficult to identify. Sandwell (pers. comm. 2013) suggested that differences could be due to edge effects that arose when the vertical offshore altimetry deflections were converted to gravity anomalies (Mitchell 2015). Nevertheless, the biases are small compared to the >100 mGal full range of the SSv23 gravity anomalies.

Free-air gravity anomalies were sampled from SSv23 along the ridge-parallel gravity profiles G1-32 located in Figure 11.2b. Because the free-air gravity field has lineations crossing the Red Sea north of 20.25°N but not south of there (Mitchell 2015), the profiles were each divided into two segments either side of 20.25°N. Those segmented gravity profiles were then inverted for basement depth variations as described below.

11.3.2.2 Bouguer slab formula

The gravity anomaly caused by a layer of infinite lateral extent and constant thickness h and density contrast $\Delta\rho$ with its surrounding material can be computed using the Bouguer slab formula:

$$\delta_g = 2\pi Gh\Delta\rho \quad (11.1)$$

where G is the gravitational constant.

To use equation (11.1) to invert the gravity data for basement relief, we have assumed a simplified structure of water underlain by evaporite and other sediments of uniform density, in turn underlain by crust and mantle also each of uniform density. As the lines are parallel to the axis, temperature in the upper mantle is expected to vary only modestly and gradually along each line, and hence we can ignore its effect on the gravity variations. In the central Red Sea, a 200-300 m thick layer of Plio-Pleistocene sediment overlies the Miocene evaporites (Egloff et al. 1991; Izzeldin 1987; Whitmarsh et al. 1974). However, it is almost uniform in thickness (Mitchell et al. 2017; Ross and Schlee 1973) and has a similar density to the underlying evaporites (Mitchell et al. 2010; Wheildon et al. 1974), so little error is introduced by using a single density for both units. If the crust is oceanic, its upper layer (seismic layer 2) comprises low-density lavas and dykes (Searle 2013). We have chosen to ignore this layer in the calculations and instead use a uniform gabbro density in the inversion because a global study of seismic refraction data revealed that variations in crustal thickness arise mainly from variations in the gabbro layer, while the lavas and dykes are more uniform (Mutter and Mutter 1993). Hence, the effect of the latter on the gravity variations should be small. Similarly, the gabbroic layer was also considered

to have uniform density, because seismic refraction data typically show little variation in seismic velocity (Grevemeyer and Weigel 1996). This may be less true of transform valleys (White and Williams 1986) although we do not interpret major offsets of the ridge and hence transform faults in this area (Okwokwo et al. 2022). The effect of topography of the Moho is ignored due to its smaller density contrast and greater depth. We return to some of these assumptions later.

Using equation (11.1), the free-air anomaly variation along the axis-parallel profiles can then be expressed in the following form:

$$g_{faa} = 2\pi G[h_w(\rho_w - \rho_c) + t_{es}(\rho_e - \rho_c)] + c \quad (11.2)$$

Where g_{faa} is free-air anomaly, h_w is water depth, t_{es} is total thickness of the evaporites and other sediments, ρ_w and ρ_c are water and crustal densities, ρ_e is the mean density of the evaporite and sediment layers, and c is a constant along each ridge-parallel gravity profile.

A mean density of 2148 kg m⁻³ was used for the evaporite and sediment layers (Wheildon et al. 1974). As the crust was assumed to have a density typical of gabbro, a density of 2957 kg m⁻³ was used for the oceanic crust based on DSDP sample measurements of Hyndman and Drury (1977). A 1020 kg m⁻³ density was used for the seawater.

By rearranging equation (11.2), we obtain:

$$t_{es} = \frac{g_{faa-c}}{2\pi G(\rho_e - \rho_c)} - h_w \frac{\rho_w - \rho_c}{\rho_e - \rho_c} \quad (11.3)$$

Hence, the basement depth is:

$$h_b = h_w + t_{es} = \frac{g_{faa-c}}{2\pi G(\rho_e - \rho_c)} + h_w \frac{\rho_e - \rho_w}{\rho_e - \rho_c} \quad (11.4)$$

Although absolute basement depths cannot be calculated from gravity anomalies alone using equation (11.4) because c is unknown, the basement depths in Figure 11.3 derived from seismic data were used to determine c for each profile.

The basement depths computed from equation (11.4) were then used to estimate basement roughness along the ridge-parallel gravity profiles.

11.3.2.3 Gravity forward modelling

Basement relief derived using the Bouguer slab formula will be underestimated, because the assumption of an infinite slab is not fully met. We have used gravity forward modelling to assess the bias magnitude, which can then be used to correct the roughness values. Forward models of free-air gravity anomalies were computed along profiles G1-32 (Figure 11.2b) by summing the gravitational effects of elementary mass rectangular cells.

The vertical gravitational attraction of a small rectangular bar of infinite length is (Shengye and Yuling 2004):

$$\Delta g = G\rho[(x+a)\ln\frac{(x+a)^2+H^2}{(x+a)^2+h^2} - (x-a)\ln\frac{(x-a)^2+H^2}{(x-a)^2+h^2} + 2H\left(\tan^{-1}\frac{x+a}{H} - \tan^{-1}\frac{x-a}{H}\right) - 2h\left(\tan^{-1}\frac{x+a}{h} - \tan^{-1}\frac{x-a}{h}\right)]$$

(11.5)

where x is horizontal distance perpendicular to the bar (with origin at the centre of the bar), $2a$ is bar width, h is depth to the upper boundary, H is depth to the lower boundary of the bar, and \tan^{-1} is the inverse tangent or arctan operator.

Based on the principle of superposition, the vertical gravitational attraction of a geological body can be reproduced by the sum of the attractions of many small individual rectangular bars constituting the body (Blakely 1996). To derive the forward models, equation (11.6) was applied to compute the sum of those gravitational attractions:

$$A_{m \times n} \times \rho_{n \times 1} = \Delta g_{m \times 1} \quad (11.6)$$

where $A_{m \times n}$ is the coefficient matrix in which elements represent how each bar contributes to the vertical gravitational attraction at each measurement point (there are n bars and m measurement points). This matrix was computed from equation (11.5).

$\rho_{n \times 1}$ is a matrix in which each element represents the density of each bar.

$\Delta g_{m \times 1}$ is a matrix in which each element represents the sum of gravitational attractions at each measurement point.

The density model in [Figure 11.8a](#) for gravity profile G21 was obtained using the modified Bouguer slab formula (equation 11.4) to estimate the evaporite/basement depth and with bathymetry to constrain the top two interfaces (water-sediments and sediments-evaporites), given the similar densities of the Plio-Pleistocene sediments to those of the evaporites mentioned earlier. The densities of seawater, evaporites and oceanic crust were assigned the same values as in Section 11.3.2.2. The forward model in [Figure 11.8b](#) was derived from the density structure in [Figure 11.8a](#) using equations (11.5) and (11.6). It tends to underestimate the extremes of gravity anomalies (peaks and troughs). After scaling the basement relief by a factor of 1.3 (i.e., maintaining the same mean depth but increasing the rugosity about that mean depth), the calculated forward model does a better job of reproducing the observed free-air anomalies. We conclude that the calculation error using the gravity slab formula is ~30%. In order to obtain more accurate basement roughness values from the slab formula, the roughness values were therefore multiplied by a factor of 1.3, as shown by the red symbols in [Figure 11.9](#). Strictly speaking, the scaling factor should vary with structure wavelength, although in practice we are studying variations in basement roughness with distance from the axis and do not expect major systematic changes in structure wavelength.

11.3.3 Bathymetry data

Version 18.1 of the Smith and Sandwell (1997) bathymetry data used in this study is shown in [Figure 11.1](#). These data were derived by combining shipboard depth measurements with, in areas lacking shipboard depth measurements, variations

inferred from the effect of the seabed density contrast on free air anomalies, in turn derived from satellite altimetry measurements. As the density of ship tracks along the centre of the Red Sea is high, however, the high relief areas around the rift axis are well constrained by survey data rather than gravity-based interpolation. Seabed depths sampled along the gravity profiles were used in inverting basement depths with equation (11.4).

11.4 Results

11.4.1 Basement roughness along across-ridge seismic profiles

The relationship between basement roughness and filter width is shown in Figure 11.4d. The mean roughness values derived from data both north and south of 20.25°N increase from 120 m at the filter width of 10 km. For filter widths of less than 70 km, the mean roughness values in the northern and southern regions are similar. Where the filter width is greater than 70 km, the roughness value of the northern region is slightly higher than that of the southern region, reaching 460 m at a filter width of 240 km. As outlined previously based on various evidence (Shi et al. 2018), the minimum in basement elevations at a ~ 60 km distance either side of the axis (Figure 11.4a) is interpreted as the continent-ocean boundary. We therefore suggest that 60 km is the most appropriate filter width to use here and so the roughness value of 230 m is our preferred estimate for the central Red Sea.

Figure 11.5 shows the relationship between the basement roughness and spreading rate for the central Red Sea together with other ridges spreading at ultraslow and slow

rates from Sauter et al. (2018). The roughness values at ultraslow spreading ridges range from 100 to >500 m, while those at slow spreading ridges are 200-240 m. The Red Sea basement roughness value (230 m) is generally consistent with these data. It lies near the curve of Malinverno's (1991) global study of abyssal hill roughness and the curve of Ehlers and Jokat (2009) of abyssal hills near hotspots.

11.4.2 Basement roughness along the ridge-parallel gravity profiles

In Figures 11.9a and 11.9b, the basement roughness values in both areas range from 200 m to 550 m and are comparable to those of the Mid-Atlantic Ridge (horizontal pink lines in Figure 11.9). As the Southwest Indian Ridge has a similar ultra-slow spreading rate to the Red Sea, we also show basement roughness values obtained from four profiles drawn parallel to that ridge axis at 14°E to 25°E and at 20-40 km from the axis. That ridge area was surveyed mainly with multibeam sonars (Grindlay et al. 1998) and has a similar segmented structure lacking major transform faults to the central Red Sea (Mitchell and Park 2014; Mitchell 2015). After detrending those profiles, the residual (root-mean-square) roughnesses are 282-415 m, slightly higher on average than those of the Mid-Atlantic Ridge, but overlapping well with the results of the gravity inversion for the central Red Sea.

The roughness values around the spreading axis are higher than those nearer to the coasts. Minima in roughness values occur about mid-way between the coast and the spreading axis (40-90 km off-axis), coinciding with the transition in crustal type from stretched continental to predominantly oceanic interpreted by Izzeldin (1982, 1987) and Shi et al. (2018).

11.5 Discussion

We have shown that both along-axis and across-axis basement roughness values in the central Red Sea overlap with those of ultraslow and slow spreading ridges. We explore here some origins of variations in these basement roughness values.

11.5.1 Transitions in basement roughness from axis towards coasts

The central Red Sea is segmented with small-offset discontinuities separating spreading segments (Searle and Ross 1975), which typically do not have well-developed transform faults or potentially no transform faults (Searle 2013). In such ridge sections near to axes, the along-axis roughness could be affected by three-dimensional effects of mantle upwelling (Rabinowicz et al. 1993) or faulting at inside corners of ridge offsets (Buck et al. 2005). Augustin et al. (2021) interpreted ridges apparently crossing the central Red Sea in gravity vertical gradients as due to areas where the crust is thicker because of excess volcanism at the spreading axis, a focusing of volcanism that occurs at other ultra-slow spreading ridges. The roughnesses in Figure 11.9 remain high to 40 km off-axis and have comparable roughnesses to the Southwest Indian Ridge profiles, where the ridge appears similarly to have sites of focused volcanism.

From 20-40 km off-axis towards the two coasts, the roughnesses decline to minima at 60 and 40 km (west and east, respectively) in Figure 11.9a and to 60 and 90 km in Figure 11.9b. These minima approximately coincide with the minima in basement

depths in the seismic profiles (Figure 11.3). A large-amplitude magnetic anomaly also occurs at about this location, which Okwokwo et al. (2022) showed is too large for a Chron 5 magnetic anomaly created by normal sea-floor spreading and may therefore arise from excess volcanic material, perhaps intrusions, emplaced at the start of sea-floor spreading. Although we cannot know the origins of the low roughnesses created then with the limited data available, it is interesting that roughnesses progressively increased towards the modern ridge axis. This may be due to volcanism at the segment centres located by Augustin et al. (2021) progressively growing and leading to greater along-axis relief. Alternatively, the intrusions responsible for the c. Chron 5 anomaly have obscured basement tectonic relief.

Beyond those oceanic-continental crustal transitions, the computed roughnesses will likely be too low because the gabbro density is inappropriate for average continental crust (although the adjacent shield rocks contain some lithologies of high density (Stern and Johnson 2019) so the extent that this is the case is unclear). Bearing that in mind, there are high values (~400 m) near the Arabian coast in the northern area (Figure 11.9a) and near the African coast in the southern area (Figure 11.9b), whereas basement roughness is much lower near the southern Arabian coast (<200 m). The along-axis roughness of the stretched continental crust appears to be asymmetric in the south. This reflects an area of smoother free-air anomalies in the SE of Figure 11.2. Besides that area, the high rugosities presumably represent relief of rifted continental crustal basement along-rift, which in part was inherited from the active rift phase, although we can't rule out some of the apparent roughness arising from varied density of the stretched continental crust.

11.5.2 Segmentation structure in reduced-to-pole magnetic anomalies

Figure 11.10 shows the aeromagnetic data originally presented by Izzeldin (1982, 1987, 1989) after reduction to the pole (RTP). Izzeldin (1987) interpreted spreading anomalies up to Chron 2A north of 20°N and up to Chron 3A south of 20°N from these data. Although less easily identified, linear anomalies also exist further from the axis, and they lie parallel with and are symmetrical about the axis (Okwokwo et al. 2022). That symmetry and their lack of correlation with basement topography (Figure 11.3) is an indication that they are seafloor-spreading anomalies, similar to anomalies in the southern Red Sea (Hall 1989).

Okwokwo et al. (2022) calculated crustal magnetizations by correcting the magnetic anomalies (Figure 11.10) for the depth to basement. Those inversion results show a comparable structure with lower amplitudes near coasts suggesting that the continental lithologies have less remanent magnetism there and are not as heavily intruded with magmas containing magnetic minerals as are present in the oceanic crust. The magnetization and RTP anomaly maps clearly show an along-axis segmentation. Bands of high RTP magnetic anomalies occur adjacent to seismic lines 11 and 17 and cross the sea SW-NE (Figure 11.10). These coincide with two across-axis basement highs in vertical gravity gradients identified by Augustin et al. (2021), suggesting that they may indeed have involved a greater thickness of crust with volcanic rock containing strong remanent magnetism. However, other basement gravity trends identified by Augustin et al. (2021) are less clearly reflected in the magnetic data, for example, there is no NE-SW-elongated anomaly adjacent to seismic line 31. From these data, there is no obvious change across-axis that mimics

the change in basement roughness (Figure 11.9) in a straightforward way. That is, if volcanism at segment centres grew progressively, it is not strongly reflected in the magnetizations. This perhaps is a result of the timing of magnetic source emplacements with varied geomagnetic field direction.

11.5.3 Along-axis gradients in mantle Bouguer gravity anomalies and along-axis roughness

Mantle Bouguer anomalies (MBAs) are marine Bouguer gravity anomalies in which the gravitational effect of the cooling lithospheric plate is removed from free-air anomalies as well as the effect of the seabed density contrast (Grindlay et al. 1998; Lin and Morgan 1992). As MBAs vary with varied crustal thickness and/or upper mantle densities, they are commonly interpreted in terms of the three-dimensional upwelling structure of the mantle beneath ridges (Magde and Sparks 1997). (As regions of upwelling mantle are hot, and hence less dense, they reduce gravity anomalies. In addition, crust is generally thicker above such regions because of greater melting, which also reduces the MBA.) Wang and Cochran (1995) measured along-axis gradients in MBA by dividing the peak to trough amplitude by distance and found them to be $\sim 0.1 \text{ mGal km}^{-1}$ at mid-ocean ridges with axial highs including the slow-spreading Reykjanes Ridge, while finding MBAs at slow spreading ridges not affected by mantle hotspots to be higher (e.g., gradients along parts of the Mid-Atlantic Ridge away from hotspots are $0.3\text{-}1.2 \text{ mGal km}^{-1}$ and those along the Southwest Indian Ridge are $0.4\text{-}0.7 \text{ mGal km}^{-1}$) (Figure 11.11).

We have computed differences in MBAs between the seismic reflection profiles where they cross the spreading axis, using the depth of basement in those profiles as a constraint, along with the seabed reflection where the axis is covered with evaporites and other sediments. Mantle Bouguer anomalies along 11 seismic profiles (Figure 11.3b) in the central Red Sea were computed by subtracting gravity effects of evaporite-crust and crust-mantle interfaces from the marine Bouguer gravity anomalies of Mitchell et al. (2017), assuming a uniform 7 km thick crust. Densities of 2148 kg m^{-3} (Wheildon et al. 1974), 2957 kg m^{-3} (Hyndman and Drury 1977), and 3220 kg m^{-3} (Crough 1983; Gvirtzman et al. 2016) were used for evaporites, oceanic crust, and mantle, respectively. As the differences were calculated along the spreading axis, consistently on zero age crust, no lithospheric cooling component was needed. Figure 11.11 shows those differences converted to along-axis gradients in MBA, which range from 0.02 to 0.3 mGal km^{-1} . Given that the seismic lines are not optimally located for sampling the largest along-axis MBA gradients (the seismic lines are spaced typically $\sim 50 \text{ km}$ (Figure 11.2), whereas peaks and troughs in MBA profiles can be 20 km or less (Magde and Sparks 1997), the 0.3 mGal km^{-1} value is the most representative of the steepest values.

A 0.1 mGal km^{-1} value was found by Wang and Cochran (1995) for the Reykjanes Ridge, where crustal thicknesses have been made relatively uniform by along-axis flow of material in the hot lower crust and/or mantle (Bell and Buck 1992). The 0.3 mGal km^{-1} value for the central Red Sea is larger, suggesting that crustal thickness is less uniform along-axis. The geochemistry of basaltic lavas ($\text{Na}_{8.0}$) also suggests that the present axis has a normal or only modestly thick crust (Haase et al. 2000). The axial depth of $\sim 2000 \text{ m}$ (Mitchell and Park 2014) is only modestly shallower than the

global average 2700 m (Parsons and Sclater 1977). Furthermore, some seismic tomography results indicate that the hot material from the Afar plume has mainly propagated under western Arabia rather than the central Red Sea at this latitude (Chang and Van der Lee 2011). With that context, our preferred across-axis roughness value (Figure 11.5) is in line with a modestly warmer crust without the extreme relief seen at the Arctic ridge or parts of the Southwest Indian Ridge. The larger MBA gradients than for the Reykjanes Ridge (Figure 11.11) would suggest that some of the along-axis roughness in Figure 11.9 does arise from varied supply of melt from the mantle (Augustin et al. 2021).

11.6 Conclusion

To further assess the structure of crust in the central Red Sea, we computed basement roughness values in profiles both across and parallel to the axis and compared them with those observed at ultraslow and slow spreading ridges. Basement roughness values from axis-crossing seismic data are ~230 m (average best estimate), similar to the values observed at other ultraslow and slow spreading ridges (e.g., the Mid-Atlantic Ridge, the Sheba Ridge, and the Southwest Indian Ridge). The roughness values derived from axis-parallel profiles of the gravity field (200-550 m) are comparable with those of the Southwest Indian Ridge where it has similar along-axis segmentation. Minima in those roughness values roughly mid-way between the coast and the spreading axis on both sides of the ridge coincide roughly with the transition in crustal type from stretched continental to predominantly oceanic. The increase in roughness values from there to the ridge axis suggests a progressive development of topography related to volcanism focused at segment centres and hence a progressive

development of those magmatic systems. Overall, the results suggest that within ~60 km of the axis, the basement is an axial ridge that has been moderately influenced by the Afar hotspot, leaving it with some along-axis segmentation and a roughness in cross-axis profiles that is typical of ultra-slow spreading centres nearer to hotspots than cold spots.

Acknowledgments

We thank David Sandwell and Walter Smith for leading the gravity and bathymetry mapping initiatives, and for the group involved in producing the grids used in our study. Figures were prepared using GMT software (Wessel et al. 2013). LMK was supported by a Royal Society of Edinburgh Personal Research Fellowship funded by the Scottish Government. We also thank John Goff, Jenny Collier and an anonymous reviewer for comments on an earlier version of this chapter, which were very helpful in revising it.

References

- Augustin, N., Devey, C.W., van der Zwan, F.M., Feldens, P., Tominaga, M., Bantan, R.A., and T. Kwasnitschka. 2014. The rifting to spreading transition in the Red Sea. *Earth Planet Sci Lett* 395:217-230.
- Augustin, N., F. M. van der Zwan, C. W. Devey, and B. Brandsdóttir. 2021. 13 million years of seafloor spreading throughout the Red Sea Basin. *Nature Comm* 12, art. 2427.

- Augustin, N., van der Zwan, F.M., Devey, C.W., Ligi, M., Kwasnitschka, T., Feldens, P., Bantan, R.A., and A.S. Basaham. 2016. Geomorphology of the central Red Sea Rift: Determining spreading processes. *Geomorphology* 274:162-179.
- Bell, R., and W. Buck. 1992. Crustal control of ridge segmentation inferred from observations of the Reykjanes Ridge. *Nature* 357:583-586.
- Bird, R.T., and R.A. Pockalny. 1994. Late Cretaceous and Cenozoic seafloor and oceanic basement roughness: Spreading rate, crustal age and sediment thickness correlations. *Earth Planet Sci Lett* 123:239-254.
- Blakely, R.J. 1996. *Potential theory in gravity and magnetic applications*. Cambridge: Cambridge University Press
- Bonatti, E. 1985. Punctiform initiation of seafloor spreading in the Red Sea during transition from a continental to an oceanic rift. *Nature* 316:33-37.
- Bosworth, W., and K. McClay. 2001. Structural and stratigraphic evolution of the Gulf of Suez rift, Egypt: a synthesis. *Mémoires du Muséum national d'histoire naturelle* 186:567-606.
- Buck, W. R., L. L. Lavier, and A. N. B. Poliakov. 2005. Modes of faulting at mid-ocean ridges. *Nature* 434:719-723.
- Chang, S-J., and S. Van der Lee. 2011. Mantle plumes and associated flow beneath Arabia and East Africa. *Earth Planet Sci Lett* 302:448-454
- Chu, D., and R.G. Gordon. 1998. Current plate motions across the Red Sea. *Geophys J Int* 135:313-328.
- Cochran, J., and G. Karner. 2007. Constraints on the deformation and rupturing of continental lithosphere of the Red Sea: the transition from rifting to drifting. *Geological Society London, Special Publications* 282:265-289.
- Cochran, J.R. 1983. A model for development of Red Sea. *AAPG Bulletin* 67:41-69.

- Cochran, J.R. 2005. Northern Red Sea: nucleation of an oceanic spreading center within a continental rift. *Geochem Geophys Geosyst* 6:Q03006. doi:10.1029/2004GC000826.
- Cochran, J.R., and F. Martinez. 1988. Evidence from the northern Red Sea on the transition from continental to oceanic rifting. *Tectonophysics* 153:25-53.
- Crough, S.T. 1983. The correction for sediment loading on the seafloor. *J Geophys Res, Solid Earth* 88:6449-6454.
- d'Acremont, E., Leroy, S., Maia, M., Gente, P., and J. Autin. 2010. Volcanism, jump and propagation on the Sheba ridge, eastern Gulf of Aden: segmentation evolution and implications for oceanic accretion processes. *Geophys J Int* 180:535-551.
- Davies, D., and C. Tramontini. 1970. The deep structure of the Red Sea. *Phil Trans Roy Soc London A, Math Phys Eng Sci* 267:181-189.
- DeMets, C., Gordon, R.G., Argus, D., and S. Stein. 1990. Current plate motions. *Geophys J Int* 101:425-478.
- DeMets, C., Gordon, R.G., and D.F. Argus. 2010. Geologically current plate motions. *Geophys J Int* 181:1-80.
- Dyment, J., Tapponnier, P., Afifi, A., Zinger, M., Franken, D., and E. Muzaiyen. 2013. A new seafloor spreading model of the Red Sea: Magnetic anomalies and plate kinematics. *AGU Fall Meeting Abstracts* T21A-2512.
- Egloff, F., Rihm, R., Makris, J., Izzeldin, Y.A., Bobsien, M., Meier, K., Junge, P., Noman, T., and W. Warsi. 1991. Contrasting structural styles of the eastern and western margins of the southern Red Sea - the 1988 Sonne Experiment. *Tectonophysics* 198:329-353. doi:10.1016/0040-1951(91)90159-P

- Ehlers, B.-M., and W. Jokat. 2009. Subsidence and crustal roughness of ultra-slow spreading ridges in the northern North Atlantic and the Arctic Ocean. *Geophys J Int* 177:451-462.
- Ghebreab, W. 1998. Tectonics of the Red Sea region reassessed. *Earth-Sci Rev* 45:1-44.
- Girdler, R.W. 1984. The evolution of the Gulf of Aden and Red Sea in space and time. *Deep Sea Res Part A Oceanographic Res Pap* 31:747-762.
- Girdler, R.W., and T.C. Southren. 1987. Structure and evolution of the northern Red Sea. *Nature* 330:716-721
- Girdler, R.W., and P. Styles. 1974. Two-stage Red Sea floor spreading. *Nature* 247:7-11.
- Girdler, R.W., and R.B. Whitmarsh. 1974. Miocene evaporites in Red Sea cores, their relevance to the problem of the width and age of oceanic crust beneath the Red Sea. In: *Initial Reports of the Deep Sea Drilling Project*, ed. R.B. Whitmarsh, O.E. Weser, D.A. Ross, et al., 23:913-921. Washington: Government Printing Office.
- Goff, J.A. 1991. A global and regional stochastic analysis of near-ridge abyssal hill morphology. *J Geophys Res, Solid Earth* 96:21713-21737.
- Goff, J.A., and T.H. Jordan. 1988. Stochastic modeling of seafloor morphology: Inversion of Sea Beam data for second-order statistics. *J Geophys Res* 93:13589-13608.
- Goff, J.A., Tucholke, B.E., Lin, J., Jaroslow, G.E., and M.C. Kleinrock. 1995. Quantitative analysis of abyssal hills in the Atlantic Ocean: A correlation between inferred crustal thickness and extensional faulting. *J Geophys Res, Solid Earth* 100:22509-22522.

- Grevenmeyer, I., and W. Weigel. 1996. Seismic velocities of the uppermost igneous crust versus age. *Geophys J Int* 124:631-635.
- Grindlay, N.R., Madsen, J.A., Rommevaux-Jestin, C., and J. Sclater. 1998. A different pattern of ridge segmentation and mantle Bouguer gravity anomalies along the ultra-slow spreading Southwest Indian Ridge (15 30' E to 25 E). *Earth Planet Sci Lett* 161:243-253.
- Guennoc, P., Pautot, G., and A. Coutelle. 1988. Surficial structures of the northern Red Sea axial valley from 23°N to 28°N: time and space evolution of neo-oceanic structures. *Tectonophysics* 153:1-23.
- Gvirtzman, Z., Faccenna, C., and T.W. Becker. 2016. Isostasy, flexure, and dynamic topography. *Tectonophysics* 683:255-271.
- Haase, K.M., Mühe, R., and P. Stoffers. 2000. Magmatism during extension of the lithosphere: geochemical constraints from lavas of the Shaban Deep, northern Red Sea. *Chem Geol* 166:225-239.
- Hall, S.A. 1989. Magnetic evidence for the nature of the crust beneath the southern Red Sea. *J Geophys Res, Solid Earth* 94:12267-12279.
doi:10.1029/Jb094ib09p12267
- Hofmann, C., Courtillot, V., Feraud, G., Rochette, P., Yirgu, G., Ketefo, E., and R. Pik. 1997. Timing of the Ethiopian flood basalt event and implications for plume birth and global change. *Nature* 389:838-841.
- Hyndman, R., and M. Drury. 1977. Physical properties of basalts, gabbros, and ultramafic rocks from DSDP Leg 37. In: *Initial Reports of the Deep Sea Drilling Project*, ed. F. Aumento, W.G. Melson, et al., 37:395-401. Washington: Government Printing Office.

- Izzeldin, A.Y. 1982. On the structure and evolution of the Red Sea. PhD Diss., Univ Strasbourg.
- Izzeldin, A.Y. 1987. Seismic, gravity and magnetic surveys in the central part of the Red Sea: their interpretation and implications for the structure and evolution of the Red Sea. *Tectonophysics* 143:269-306.
- Izzeldin, A.Y. 1989. Transverse structures in the central part of the Red Sea and implications on early stages of oceanic accretion. *Geophys J Int* 96:117-129.
- Karbe, L. 1987. Hot brines and the deep sea environment. In: *Key Environment, Red Sea*, ed. A.J. Edwards, and S.M. Head, 70-89. Oxford: Pergamon Press.
- Kozdroj, W., Kattan, F.H., Kadi, K.A., Al Alfy, Z.S.A., Qweiss, K.A., and M.M. Mansour. 2012. SGS-EMRA project for Trans-Red Sea correlation between the Central Eastern Terrane (Egypt) and Midyan Terrane (Saudi Arabia). Saudi Geol Surv Tech Report SGS-TR-2011-5, 62 p, 65 pls.
- Lagabrielle, Y., Ruellan, E., Tanahashi, M., Bourgois, J., Buffet, G., de Alteriis, G., Dymont, J., Goslin, J., Grácia-Mont, E., and Y. Iwabushi. 1996. Active oceanic spreading in the northern North Fiji Basin: results of the NOFI cruise of R/V L'Atalante (Newstarmer Project). *Marine Geophys Res* 18:225-247.
- Levi, S., and R. Riddihough. 1986. Why are marine magnetic anomalies suppressed over sedimented spreading centers? *Geology* 14:651-654.
- Ligi, M., Bonatti, E., Tontini, F.C., Cipriani, A., Cocchi, L., Schettino, A., Bortoluzzi, G., Ferrante, V., Khalil, S., and N.C. Mitchell. 2011. Initial burst of oceanic crust accretion in the Red Sea due to edge-driven mantle convection. *Geology* 39:1019-1022.
- Ligi, M., Bonatti, E., Bortoluzzi, G., Cipriani, A., Cocchi, L., Caratori Tontini, F., Carminati, E., Ottolini, L., and A. Schettino. 2012. Birth of an ocean in the Red

- Sea: initial pangs. *Geochem Geophys Geosyst* 13: Q08009.
doi:10.1029/2012GC004155.
- Lin, J., and J.P. Morgan. 1992. The spreading rate dependence of three-dimensional mid-ocean ridge gravity structure. *Geophys Res Lett* 19:13-16.
- Lizarralde, D., Gaherty, J.B., Collins, J.A., Hirth, G., and S.D. Kim. 2004. Spreading-rate dependence of melt extraction at mid-ocean ridges from mantle seismic refraction data. *Nature* 432:744.
- Ma, L.Y., and J.R. Cochran. 1997. Bathymetric roughness of the Southeast Indian Ridge: Implications for crustal accretion at intermediate spreading rate mid-ocean ridges. *J Geophys Res, Solid Earth* 102:17697-17711.
- Magde, L.S., and D.W. Sparks. 1997. Three-dimensional mantle upwelling, melt generation, and melt migration beneath segment slow spreading ridges. *J Geophys Res, Solid Earth* 102:20571-20583.
- Malinverno, A. 1991. Inverse square-root dependence of mid-ocean-ridge flank roughness on spreading rate. *Nature* 352:58-60.
- Malinverno, A., and L.E. Gilbert. 1989. A stochastic model for the creation of abyssal hill topography at a slow spreading center. *J Geophys Res, Solid Earth* 94:1665-1675.
- Martinez, F., and J.R. Cochran. 1988. Structure and tectonics of the northern Red Sea: catching a continental margin between rifting and drifting. *Tectonophysics* 150:1-31.
- McKenzie, D., Davies, D., and P. Molnar. 1970. Plate tectonics of the Red Sea and East Africa. *Nature* 226:243.
- Minshull, T. 1999. On the roughness of Mesozoic oceanic crust in the western North Atlantic. *Geophys J Int* 136:286-290.

- Mitchell, N.C. 2015. Lineaments in gravity data of the Red Sea. In: *The Red Sea: The formation, morphology, oceanography and environment of a young ocean basin*, ed. N.M.A. Rasul, and I.C.F. Stewart, 123-133. Berlin Heidelberg, Springer Earth System Sciences.
- Mitchell, N.C., Ligi, M., Feldens, P., and C. Hübscher. 2017. Deformation of a young salt giant: regional topography of the Red Sea Miocene evaporites. *Basin Res* 29:352-369.
- Mitchell, N.C., Ligi, M., Ferrante, V., Bonatti, E., and E. Rutter. 2010. Submarine salt flows in the central Red Sea. *Geol Soc Am Bull* 122:701-713.
- Mitchell, N.C., and Y. Park. 2014. Nature of crust in the central Red Sea. *Tectonophysics* 628:123-139. doi:10.1016/j.tecto.2014.04.029
- Mitchell, N. C., W. Shi, A. Y. Izzeldin, and I. C. F. Stewart. 2021. Reconstructing the level of the central Red Sea evaporites at the end of the Miocene. *Basin Res* 33:1266-1292. <https://doi.org/10.1111/bre.12513>.
- Mohr, P. 1983. Ethiopian flood basalt province. *Nature* 303:577-584.
- Mutter, C.Z., and J.C. Mutter. 1993. Variations in thickness of layer 3 dominate oceanic crustal structure. *Earth Planet Sci Lett* 117:295-317.
- Neumann, G.A., and D.W. Forsyth. 1995. High resolution statistical estimation of seafloor morphology: Oblique and orthogonal fabric on the flanks of the Mid-Atlantic Ridge, 34-35.5 S. *Mar Geophys Res* 17:221-250.
- Okwokwo, O. I., N. C. Mitchell, W. Shi, I.C.F. Stewart, and A. Y. Izzeldin. 2022. How have thick evaporites affected early sea-floor spreading magnetic anomalies in the Central Red Sea? *Geophys J Int* 229:1550-1566.
- Omar, G.I., and M.S. Steckler. 1995. Fission track evidence on the initial rifting of the Red Sea: two pulses, no propagation. *Science* 270:1341-1344.

- Parsons, B., and J. G. Sclater. 1977. An analysis of the variation of ocean floor bathymetry and heat flow with age. *J Geophys Res* 82:803-827.
- Pautot, G., Guennoc, P., Coutelle, A., and N. Lyberis. 1984. Discovery of a large brine deep in the northern Red Sea. *Nature* 310:133.
- Phillips, J.D. 1970. Magnetic anomalies in the Red Sea. *Phil Trans Roy Soc London A, Math Phys Eng Sci* 267:205-217.
- Rabinowicz, M., S. Rouzo, J.-C. Sempere, and C. Rosemberg. 1993. Three-dimensional mantle flow beneath mid-ocean ridges. *J Geophys Res* 98:7851-7869.
- Reilinger, R., McClusky, S., and A. ArRajehi. 2015. Geodetic constraints on the geodynamic evolution of the Red sea. In: *The Red Sea: The formation, morphology, oceanography and environment of a young ocean basin*, ed. N.M.A. Rasul, and I.C.F. Stewart, 135-149. Berlin Heidelberg, Springer Earth System Sciences.
- Rihm, R., and C. Henke. 1998. Geophysical studies on early tectonic controls on Red Sea rifting, opening and segmentation. In: *Sedimentation and Tectonics in Rift Basins Red Sea-Gulf of Aden*, 29-49. Springer.
- Roeser, H.A. 1975. A detailed magnetic survey of the southern Red Sea. *Geologisches Jahrbuch* 13:131-153.
- Ross, D.A., and J. Schlee. 1973. Shallow structure and geologic development of the southern Red Sea. *Geol Soc Am Bull* 84:3827-3848.
- Ryan, W.B., Carbotte, S.M., Coplan, J.O., O'Hara, S., Melkonian, A., Arko, R., Weissel, R.A., Ferrini, V., Goodwillie, A., and F. Nitsche. 2009. Global multi-resolution topography synthesis. *Geochem Geophys Geosyst* 10:Q03014. doi:10.1029/2008GC002332

- Sandwell, D.T., Garcia, E., Soofi, K., Wessel, P., Chandler, M., and W.H. Smith. 2013. Toward 1-mGal accuracy in global marine gravity from CryoSat-2, Envisat, and Jason-1. *Leading Edge* 32:892-899.
- Sandwell, D.T., Muller, R.D., Smith, W.H.F., Garcia, E., and R. Francis. 2014. New global marine gravity model from CryoSat-2 and Jason-1 reveals buried tectonic structure. *Science* 346:65-67. doi:10.1126/science.1258213
- Sauter, D., Sloan, H., Cannat, M., Goff, J., Patriat, P., Schaming, M., and W.R. Roest. 2011. From slow to ultra-slow: How does spreading rate affect seafloor roughness and crustal thickness? *Geology* 39:911-914.
- Sauter, D., Tugend, J., Gillard, M., Nirrengarten, M., Autin, J., Manatschal, G., Cannat, M., Leroy, S., and M. Schaming. 2018. Oceanic basement roughness alongside magma-poor rifted margins: insight into initial seafloor spreading. *Geophys J Int* 212:900-915. doi:10.1093/gji/ggx439
- Searle, R.C. 2013. *Mid-ocean ridges*. Cambridge University Press
- Searle, R. C., and D. A. Ross. 1975. A geophysical study of the Red Sea axial trough between 20.5° and 22°N. *Geophys J Roy Astr Soc* 43:555-572.
- Shengye, Z., and P. Yuling. 2004. *The principle of applied geophysics*. China University of Geosciences Press.
- Shi, W., Mitchell, N.C., Kalnins, L.M., and A.Y. Izzeldin. 2018. Oceanic-like axial crustal high in the central Red Sea. *Tectonophysics* 747-748:327-342. doi:/10.1016/j.tecto.2018.10.011
- Sloan, H., Sauter, D., Goff, J.A., and M. Cannat. 2012. Abyssal hill characterization at the ultraslow spreading Southwest Indian Ridge. *Geochem Geophys Geosyst* 13:Q0AE06. doi:10.1029/2011GC0038502

- Small, C. 1994. A global analysis of mid-ocean ridge axial topography. *Geophys J Int* 116:64-84.
- Smith, W.H.F., and D.T. Sandwell. 1997. Global sea floor topography from satellite altimetry and ship depth soundings. *Science* 277:1956-1962. doi:10.1126/science.277.5334.1956
- Stern, R. J., and P.R. Johnson. 2019. Constraining the opening of the Red Sea: evidence from the Neoproterozoic margins and Cenozoic magmatism for a volcanic rifted margin. In: *Geological setting, palaeoenvironment and archaeology of the Red Sea*, ed. N. M. A. Rasul, and I. C. F. Stewart, 53-79. Cham, Switzerland: Springer Nature.
- Sultan, M., Becker, R., Arvidson, R., Shore, P., Stern, R., El Alfy, Z., and Attia, R. 1993. New constraints on Red Sea rifting from correlations of Arabian and Nubian Neoproterozoic outcrops. *Tectonics* 12:1303-1319.
- Sultan, M., Becker, R., Arvidson, R.E., Shore, P., Stern, R.J., Elalfy, Z., and E.A. Guinness. 1992. Nature of the Red Sea crust: A controversy revisited. *Geology* 20:593-596.
- Tapponnier, P., Dymant, J., Zinger, M., Franken, D., Afifi, A., Wyllie, A., Ali, H., and I. Hanbal. 2013. Revisiting seafloor-spreading in the Red Sea: Basement nature, transforms and ocean-continent boundary. *AGU Fall Meeting Abst* T12B-04.
- Tramontini, C., and D. Davies. 1969. A seismic refraction survey in the Red Sea. *Geophys J Int* 17:225-241. doi:10.1111/j.1365-246X.1969.tb02323.x
- Vine, F.J. 1966. Spreading of the ocean floor: new evidence. *Science* 154:1405-1415.
- Wang, X., and J.R. Cochran. 1995. Along-axis gravity gradients at mid-ocean ridges: Implications for mantle flow and axial morphology. *Geology* 23:29-32.

- Weigelt, E., and W. Jokat. 2001. Peculiarities of roughness and thickness of oceanic crust in the Eurasian Basin, Arctic Ocean. *Geophys J Int* 145:505-516.
- Wessel, P., and A.B. Watts. 1988. On the accuracy of marine gravity measurements. *J Geophys Res* 93:393-413.
- Wessel P., W.H.F. Smith, R. Scharroo, J. Luis and F. Wobbe (2013) Generic mapping tools: improved version released. *Eos, Transactions American Geophysical Union* 94:409-410.
- Wheildon, J., Evans, T., Girdler, R., Whitmarsh, R., Weser, O., and D. Ross. 1974. Thermal conductivity, density, and sonic velocity measurements of samples of anhydrite and halite from Sites 225 and 227. In: *Initial Reports of the Deep Sea Drilling Project*, ed. R.B. Whitmarsh, O.E. Weser, D.A. Ross, et al., 23:909-911. Washington: US Government Printing Office.
- White, R.S., and C.A. Williams. 1986. Oceanic fracture zones. *J Geol Soc* 143:737-741. doi:10.1144/gsjgs.143.5.0737
- Whitmarsh, R., Weser, O., and D. Ross. 1974. *Initial Reports of the Deep Sea Drilling Project*. Washington: US Government Printing Office.

Figure captions

Figure 11.1 Bathymetry of the Red Sea (Smith and Sandwell 1997, version 18.1). Red dots locate the prominent deeps in the central Red Sea from Augustin et al. (2014) and Karbe (1987). From north to south, these are (1) Nereus, (2) Thetis, (3) Hadarba, (4) Hatiba, (5) Atlantis II, (6) Erba, (7) Port Sudan, (8) Suakin, and (9) Pelagia deeps. The relative plate motion vectors were predicted based on the poles of Chu and Gordon (1998).

Figure 11.2 (a): Free-air gravity anomalies (Sandwell et al. 2014, version 23.1) and locations of multichannel seismic reflection profiles 7, 9, 11, 15, 17, 19, 21, 25, 27, 29, 31 from Izzeldin (1982, 1987). (b): Locations of gravity profiles G1-32 and seismic reflection profiles as in (a). Cyan line approximately locates the spreading axis. Green line locates gravity profile G21, along which the gravity forward modelling results are shown in Figure 11.8. The study area was divided into two areas: north of 20.25°N and south of 20.25°N, as the free-air gravity field north of 20.25°N has cross-axis lineaments suggested to be due to oceanic spreading segments (Mitchell 2015).

Figure 11.3 Depths derived from the seismic reflection profiles of Izzeldin (1987). Line numbers are shown in the lower right corner of each panel. Magnetic anomalies (purple lines) along the seismic profiles are reduced-to-pole magnetic anomalies (Figure 11.10). Black lines denote bathymetry (Smith and Sandwell 1997, version 18.1). Dark green, cyan, and red lines are the depths of the seabed, the S-reflection at the top of the Miocene evaporites, and the basement, respectively. RTP: Reduced-to-the-pole.

Figure 11.4 (a): Basement depths along the Red Sea seismic lines (Figure 11.2a and 11.2b) corrected for the isostatic loading of evaporites and other sediments. (b): Regional crustal subsidence trend estimated from (a) using a 60 km running median average filter. (c): Residual basement reliefs obtained by removing regional crustal subsidence trend in (b) from the isostatically adjusted basement depths in (a). Grey shadings (within ~60 km of the axis) in (a), (b), and (c) show the area Shi et al. (2018)

interpreted as underlain by oceanic crust. (d): The relationship between the mean basement roughness value and filter width. Blue and black lines represent roughness values in northern (north of 20.25°N) and southern (south of 20.25°N) regions, while red line represents the values derived from data of both regions. The roughness value of 230 m at the filter width of 60 km is considered as the most appropriate value for the central Red Sea (see main text).

Figure 11.5 The relationship between the basement roughness and spreading rate for ultraslow and slow spreading ridges, modified from Sauter et al. (2018). The error bar of the Red Sea value indicates a conservative range of roughness values derived from various filter widths in Figure 11.4d. The other error bars show the standard deviations of the corresponding roughness values. SWIR: Southwest Indian Ridge, MCSC: Mid-Cayman Spreading Center, MAR: Mid-Atlantic Ridge, SPR: South Pandora Ridge. Data for the Red Sea are determined in this study. Data for Arctic ridge are from Weigelt and Jokat (2001) and Ehlers and Jokat (2009). Data for SWIR are from Sauter et al. (2011) and Sloan et al. (2012). Data for MCSC are from Sauter et al. (2018). Data for MAR are from Goff (1991), Goff et al. (1995), Neumann and Forsyth (1995), Minshull (1999), and Lizarralde et al. (2004). Data for Sheba ridge are from d'Acremont et al. (2010). Data for SPR are from Lagabrielle et al. (1996). The continuous black line is the power-law of Malinverno (1991). The dashed blue and red lines are power-laws derived by Ehlers and Jokat (2009) from basement topography adjacent to ridges with axial valleys and with axial highs, respectively.

Figure 11.6 Histograms of differences between the SSv23 and free-air anomaly data collected on (a): RRS Shackleton and (b): RV Robert Conrad (SSv23 minus shipboard value). Vertical lines show the means and standard deviations of the differences.

Figure 11.7 Left panel shows differences between the SSv23 free-air gravity field and shipboard (RRS Shackleton and RV Robert Conrad) gravity data (SSv23 minus shipboard) after the shipboard data were filtered with a 4 km along-track median filter. Right panel shows free-air gravity anomalies of SSv22, which was similar to SSv23.

Figure 11.8 Forward modelling of gravity profile G21. (a): Density model obtained from the slab-formula-based results. (b): Forward 2D model predictions of free-air gravity anomalies based on the slab formula results (red) underestimate the gravity anomaly variation (blue line is free air anomaly from satellite altimetry). After multiplying the basement relief variation by a factor of 1.3, the forward model (black line) better predicts the observations. Based on this result, the error in basement roughness derived from axis-parallel gravity profiles is 30%. The density model in (a) was subdivided into $n=3600$ small cells, and the number of measurement points m is 720.

Figure 11.9 Basement roughness values (green symbols) computed with a modified Bouguer slab formula along axis-parallel gravity profiles G1-32 (Figure 11.2b) using a crustal density (2957 kg m^{-3}) appropriate for oceanic crust dominated by gabbro. Values have been omitted where the ridge axis is largely not covered in evaporites and hence the inversion model is inappropriate. (a): North of 20.25°N . (b): South of 20.25°N . Red symbols show the values corrected for bias arising from the slab formula based on the results of gravity forward modelling (see Section 11.3.2.3). Horizontal lines represent basement roughness values calculated along lines parallel to ridges from bathymetry where the basement is only weakly sedimented and where

the bathymetry has a similar segmentation structure to the central Red Sea (bathymetry data derived from the Global Multi-Resolution Topography Synthesis (Ryan et al. 2009)). Pink lines were derived from profiles of the Mid-Atlantic Ridge over latitudes 22°N to 32°N and 80 km off-axis. Blue lines were derived from profiles of the ultra-slow spreading Southwest Indian Ridge over longitudes 14°E to 25°E and 20-40 km off-axis.

Figure 11.10 Aeromagnetic anomalies from Izzeldin (1982, 1987) and reduced to pole. Red lines locate the seismic reflection profiles (Figure 11.2a).

Figure 11.11 Comparison of along-axis gradients in mantle Bouguer anomalies (MBA) in the central Red Sea with those at other mid-ocean ridges, modified from Wang and Cochran (1995). RR: Reykjanes Ridge, CIR: Central Indian Ridge, SEIR: Southeast Indian Ridge, GSC: Galapagos spreading center, EPR: East Pacific Rise.

Figures with captions

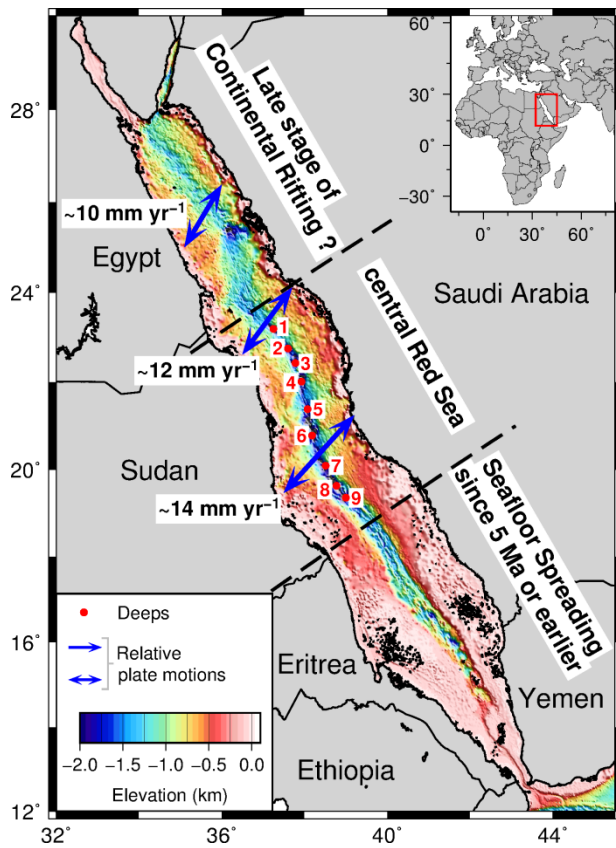


Figure 11.1 Bathymetry of the Red Sea (Smith and Sandwell 1997, version 18.1). Red dots locate the prominent deeps in the central Red Sea from Augustin et al. (2014) and Karbe (1987). From north to south, these are (1) Nereus, (2) Thetis, (3) Hadarba, (4) Hatiba, (5) Atlantis II, (6) Erba, (7) Port Sudan, (8) Suakin, and (9) Pelagia deeps. The relative plate motion vectors were predicted based on the poles of Chu and Gordon (1998).

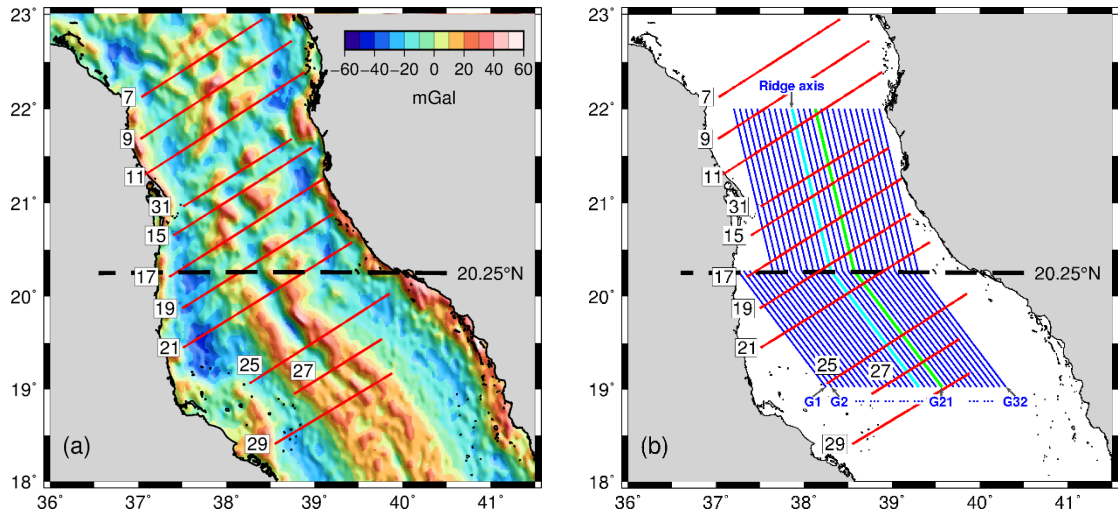


Figure 11.2 (a): Free-air gravity anomalies (Sandwell et al. 2014, version 23.1) and locations of multichannel seismic reflection profiles 7, 9, 11, 15, 17, 19, 21, 25, 27, 29, 31 from Izzeldin (1982, 1987). (b): Locations of gravity profiles G1-32 and seismic reflection profiles as in (a). Cyan line approximately locates the spreading axis. Green line locates gravity profile G21, along which the gravity forward modelling results are shown in Figure 11.8. The study area was divided into two areas: north of 20.25°N and south of 20.25°N, as the free-air gravity field north of 20.25°N has cross-axis lineaments suggested to be due to oceanic spreading segments (Mitchell 2015).

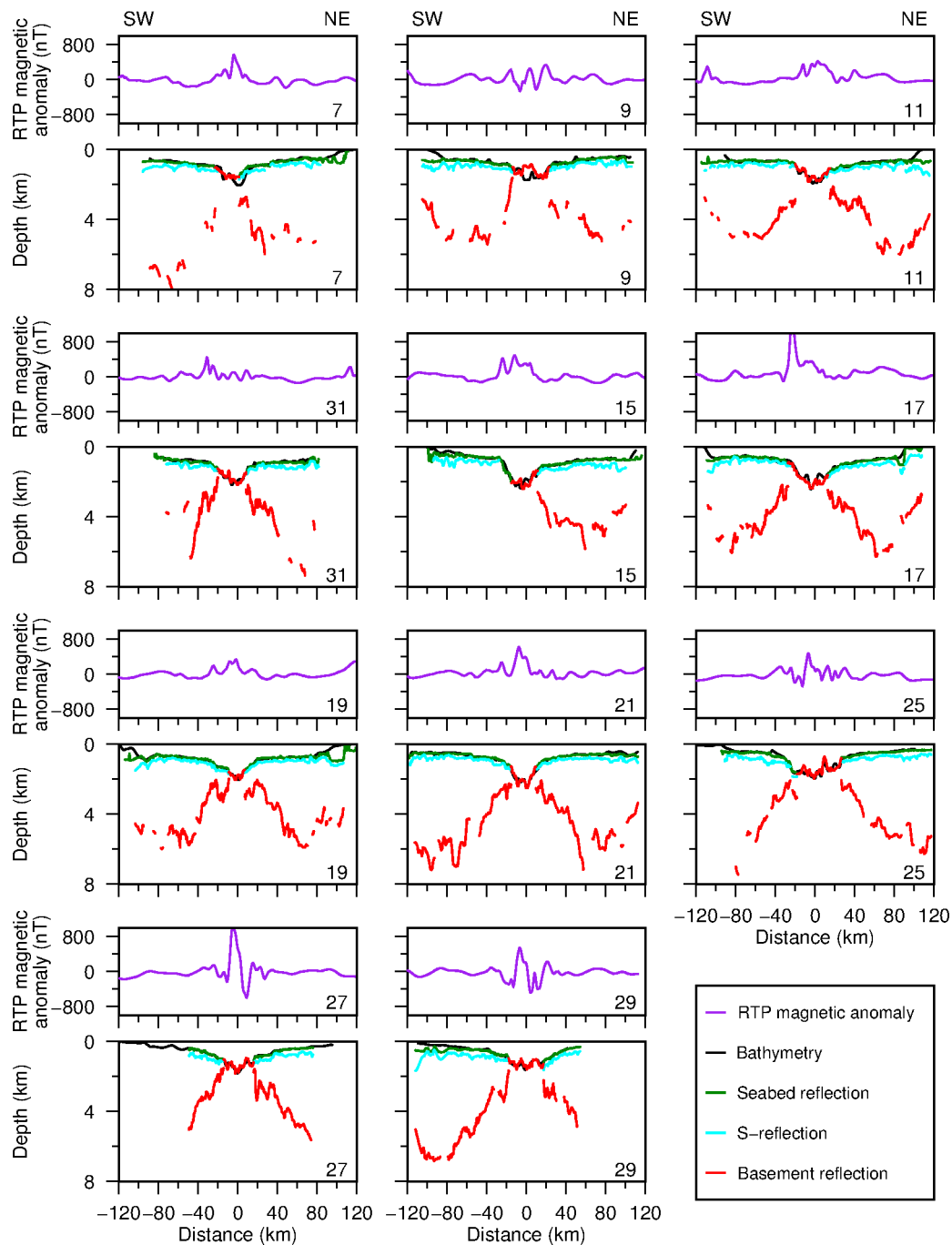


Figure 11.3 Depths derived from the seismic reflection profiles of Izzeldin (1987). Line numbers are shown in the lower right corner of each panel. Magnetic anomalies (purple lines) along the seismic profiles are reduced-to-pole magnetic anomalies (Figure 11.10). Black lines denote bathymetry (Smith and Sandwell 1997, version 18.1). Dark green, cyan, and red lines are the depths of the seabed, the S-reflection at the top of the Miocene evaporites, and the basement, respectively. RTP: Reduced-to-the-pole.

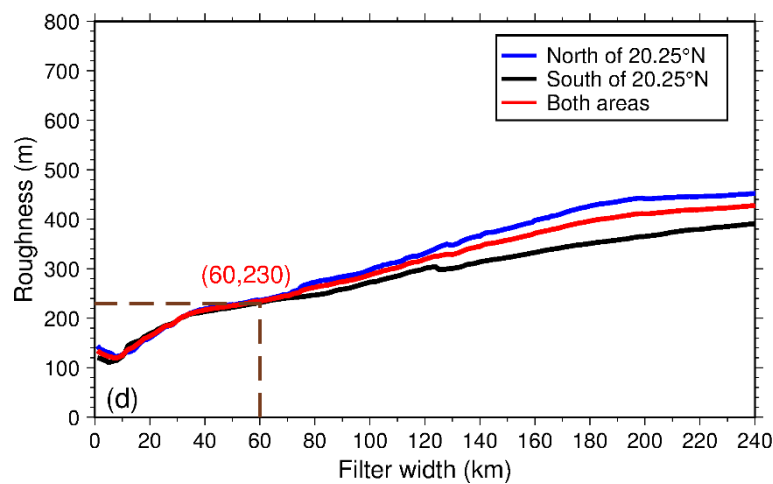
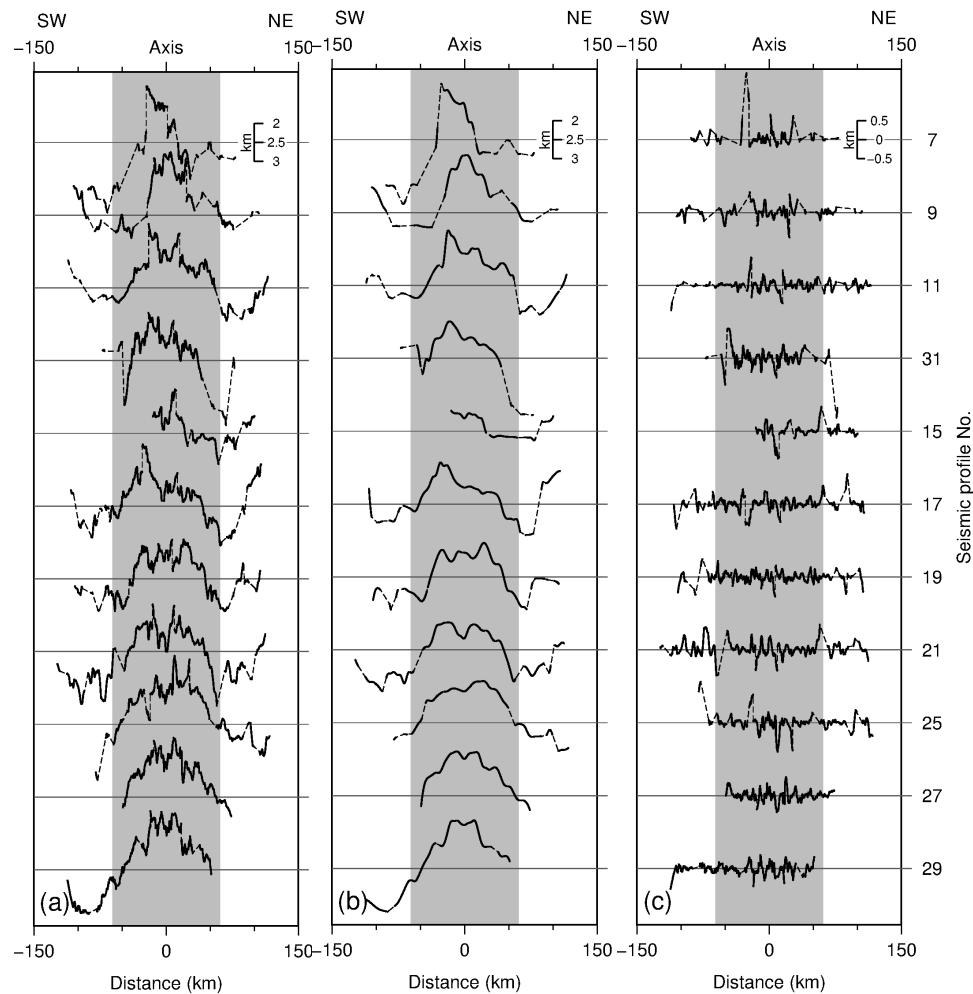


Figure 11.4 (a): Basement depths along the Red Sea seismic lines (Figure 11.2a and 11.2b) corrected for the isostatic loading of evaporites and other sediments. (b): Regional crustal subsidence trend estimated from (a) using a 60 km running median average filter. (c): Residual basement reliefs obtained by removing regional crustal subsidence trend in (b) from the isostatically adjusted basement depths in (a). Grey shadings (within ~60 km of the axis) in (a), (b), and (c) show the area Shi et al. (2018)

interpreted as underlain by oceanic crust. (d): The relationship between the mean basement roughness value and filter width. Blue and black lines represent roughness values in northern (north of 20.25°N) and southern (south of 20.25°N) regions, while red line represents the values derived from data of both regions. The roughness value of 230 m at the filter width of 60 km is considered as the most appropriate value for the central Red Sea (see main text).

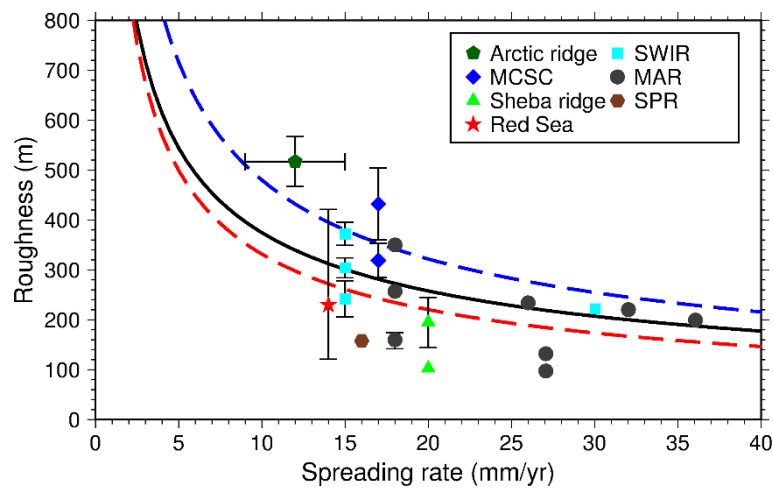


Figure 11.5 The relationship between the basement roughness and spreading rate for ultraslow and slow spreading ridges, modified from Sauter et al. (2018). The error bar of the Red Sea value indicates a conservative range of roughness values derived from various filter widths in Figure 11.4d. The other error bars show the standard deviations of the corresponding roughness values. SWIR: Southwest Indian Ridge, MCSC: Mid-Cayman Spreading Center, MAR: Mid-Atlantic Ridge, SPR: South Pandora Ridge. Data for the Red Sea are determined in this study. Data for Arctic ridge are from Weigelt and Jokat (2001) and Ehlers and Jokat (2009). Data for SWIR are from Sauter et al. (2011) and Sloan et al. (2012). Data for MCSC are from Sauter et al. (2018). Data for MAR are from Goff (1991), Goff et al. (1995), Neumann and Forsyth (1995), Minshull (1999), and Lizarralde et al. (2004). Data for Sheba ridge are from d'Acremont et al. (2010). Data for SPR are from Lagabrielle et al. (1996). The continuous black line is the power-law of Malinverno (1991). The dashed blue and red lines are power-laws derived by Ehlers and Jokat (2009) from basement topography adjacent to ridges with axial valleys and with axial highs, respectively.

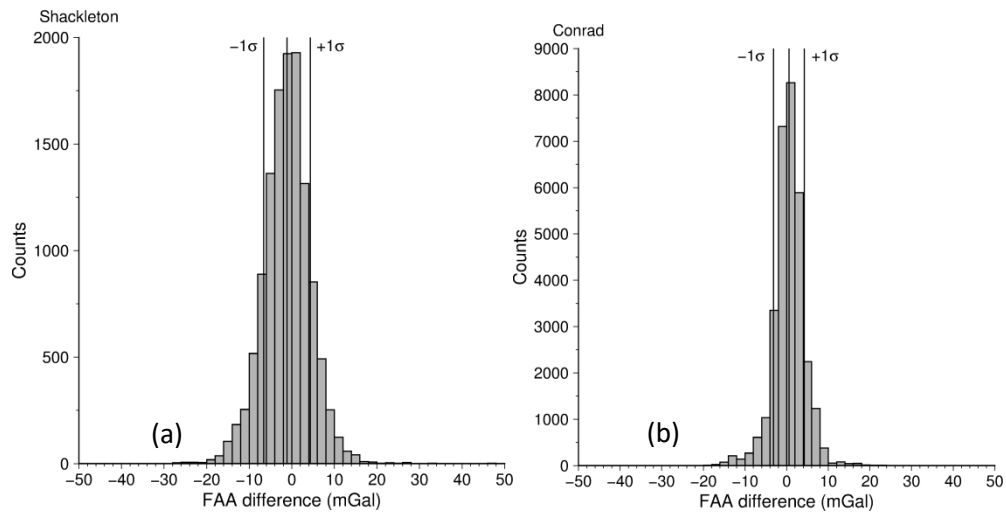


Figure 11.6 Histograms of differences between the SSv23 and free-air anomaly data collected on (a): RRS *Shackleton* and (b): RV *Robert Conrad* (SSv23 minus shipboard value). Vertical lines show the means and standard deviations of the differences.

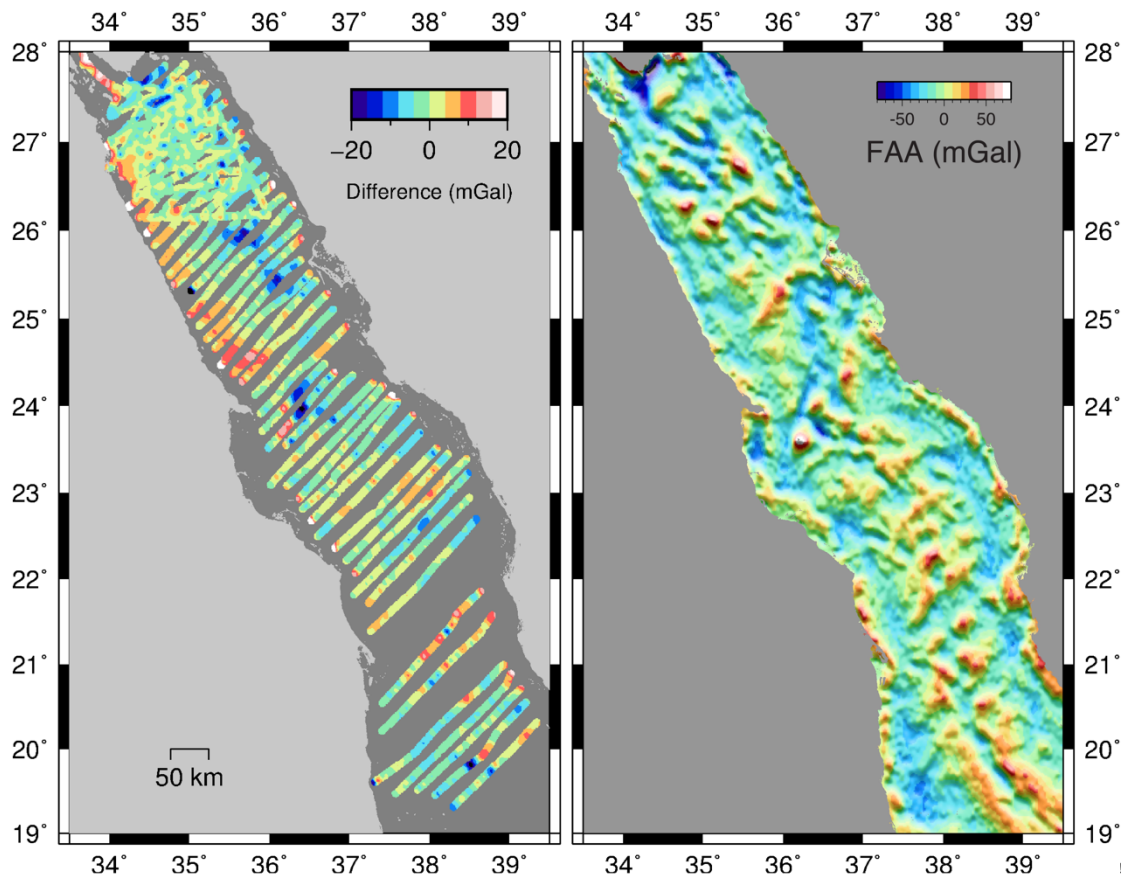
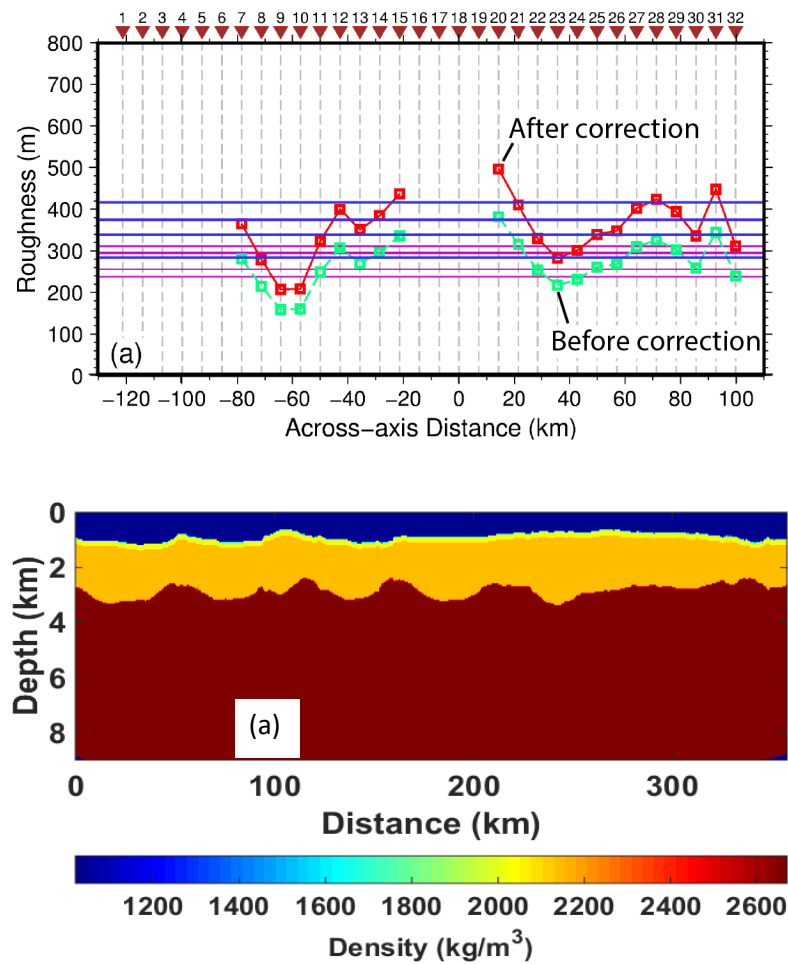


Figure 11.7 Left panel shows differences between the SSv23 free-air gravity field and shipboard (RRS *Shackleton* and RV *Robert Conrad*) gravity data (SSv23 minus shipboard) after the shipboard data were filtered with a 4 km along-track median filter. Right panel shows free-air gravity anomalies of SSv22, which was similar to SSv23.



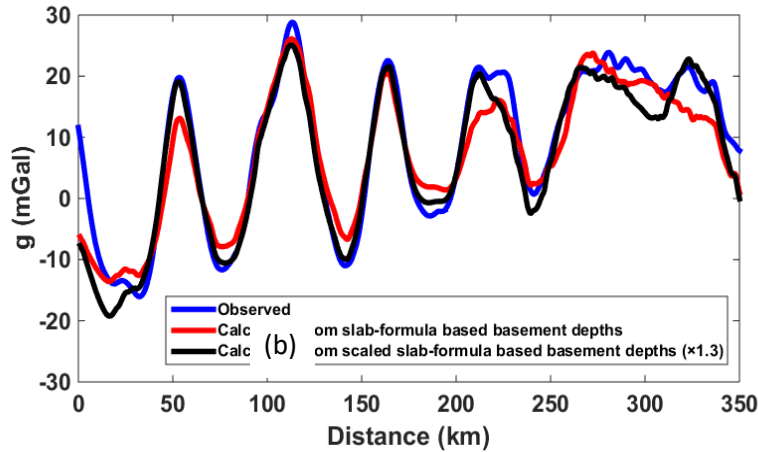
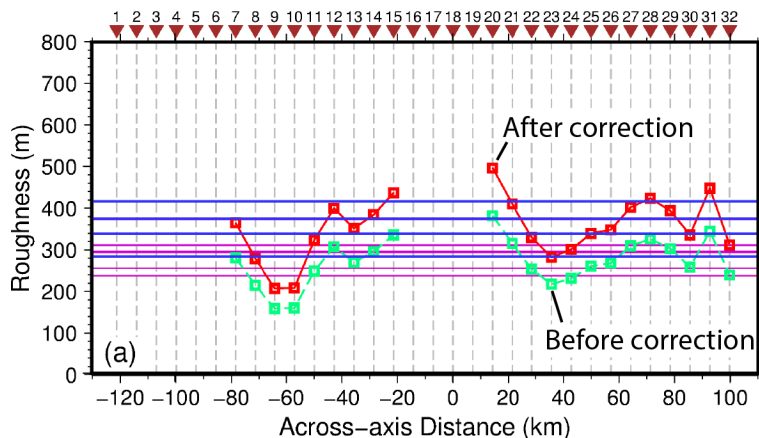


Figure 11.8 Forward modelling of gravity profile G21. (a): Density model obtained from the slab-formula-based results. (b): Forward 2D model predictions of free-air gravity anomalies based on the slab formula results (red) underestimate the gravity anomaly variation (blue line is free air anomaly from satellite altimetry). After multiplying the basement relief variation by a factor of 1.3, the forward model (black line) better predicts the observations. Based on this result, the error in basement roughness derived from axis-parallel gravity profiles is 30%. The density model in (a) was subdivided into $n=3600$ small cells, and the number of measurement points m is 720.



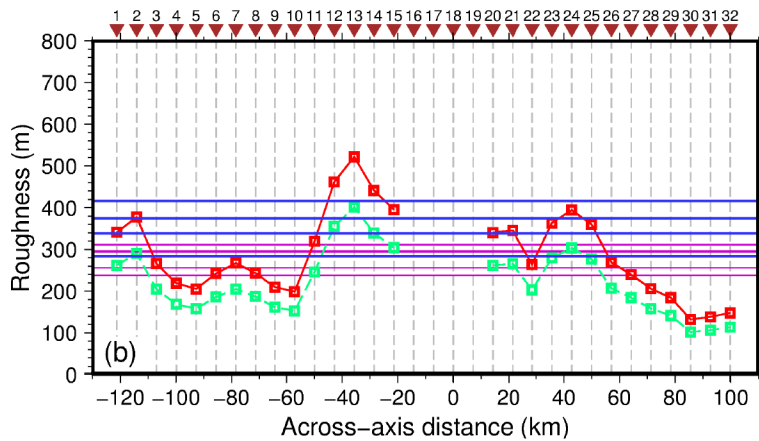


Figure 11.9 Basement roughness values (green symbols) computed with a modified Bouguer slab formula along axis-parallel gravity profiles G1-32 (Figure 11.2b) using a crustal density (2957 kg m^{-3}) appropriate for oceanic crust dominated by gabbro. Values have been omitted where the ridge axis is largely not covered in evaporites and hence the inversion model is inappropriate. (a): North of 20.25°N . (b): South of 20.25°N . Red symbols show the values corrected for bias arising from the slab formula based on the results of gravity forward modelling (see Section 11.3.2.3). Horizontal lines represent basement roughness values calculated along lines parallel to ridges from bathymetry where the basement is only weakly sedimented and where the bathymetry has a similar segmentation structure to the central Red Sea (bathymetry data derived from the Global Multi-Resolution Topography Synthesis (Ryan et al. 2009)). Pink lines were derived from profiles of the Mid-Atlantic Ridge over latitudes 22°N to 32°N and 80 km off-axis. Blue lines were derived from profiles of the ultra-slow spreading Southwest Indian Ridge over longitudes 14°E to 25°E and 20-40 km off-axis.

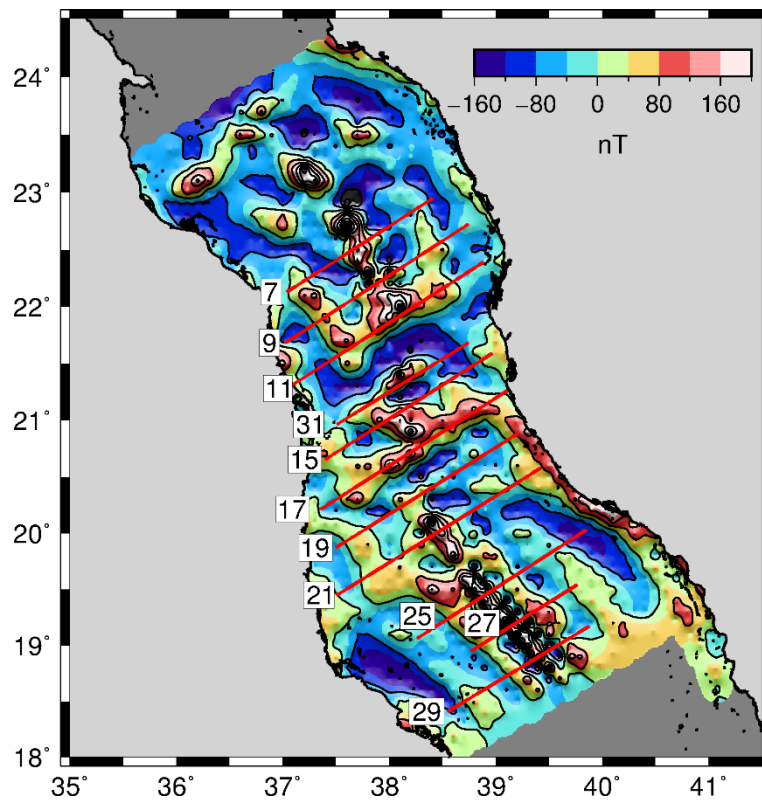


Figure 11.10 Aeromagnetic anomalies from Izzeldin (1982, 1987) and reduced to pole. Red lines locate the seismic reflection profiles (Figure 11.2a).

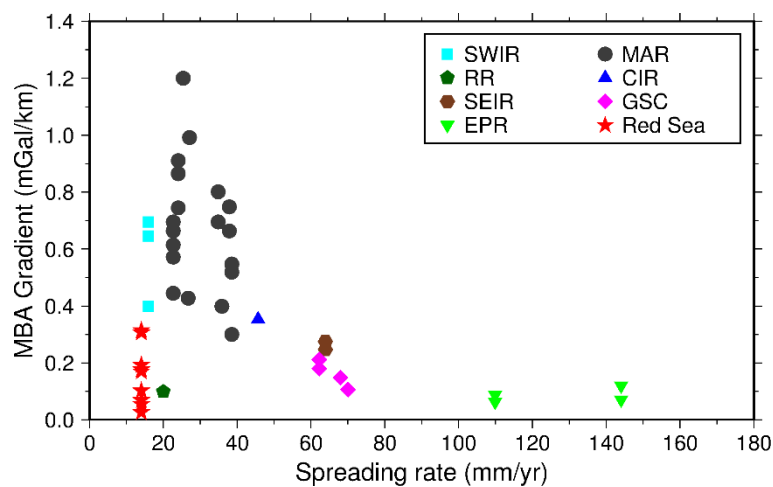


Figure 11.11 Comparison of along-axis gradients in mantle Bouguer anomalies (MBA) in the central Red Sea with those at other mid-ocean ridges, modified from Wang and Cochran (1993). RR: Reykjanes Ridge, CIR: Central Indian Ridge, SEIR: Southeast Indian Ridge, GSC: Galapagos spreading center, EPR: East Pacific Rise.